

Proof of Shock-cloud interaction within parts of γ -Cygni region

Yuan Li^{*1,2}, Gwenael Giacinti^{1,2**}, Siming Liu^{***3}, and Yi Xing⁴

¹ Tsung-Dao Lee Institute, Shanghai Jiao Tong University, Shanghai 201210, PRC

² School of Physics and Astronomy, Shanghai Jiao Tong University, Shanghai 200240, PRC

³ School of Physical Science and Technology, Southwest Jiaotong University, Chengdu 610031, PRC

⁴ Key Laboratory for Research in Galaxies and Cosmology, Shanghai Astronomical Observatory, Chinese Academy of Sciences, Shanghai 200030, PRC

December 10, 2024

ABSTRACT

We reanalyze 15 yr data recorded by the Fermi Large Area Telescope in a region around supernova remnant (SNR) γ -Cygni from 100 MeV to 1 TeV, and find that the spectra of two extended sources associated with the southeast radio SNR arc and the TeV VERITAS source can be described well by single power-laws with photon indices of 2.149 ± 0.005 and 2.01 ± 0.06 , respectively. Combining with high resolution gas observation results, we model the emission in the hadronic scenario, where the γ -ray emission could be interpreted as escaped CRs illuminating a surrounding Molecular Cloud (MC) plus an ongoing shock-cloud interaction component. In this scenario, the difference between these two GeV spectral indices is due to the different ratios of the MC mass between the escaped component and the trapped component in the two regions. We further analyze, in a potential pulsar halo region, the relationship between energy density ε_e , spin-down power \dot{E} , and the γ -ray luminosity L_γ of PSR J2021+4026. Our results indicate that the existence of a pulsar halo is unlikely. On the other hand, considering the uncertainty on the SNR distance, the derived energy density ε_e might be overestimated, thus the scenario of a SNR and a pulsar halo overlapping in the direction of the line of sight (LOS) cannot be ruled out.

Key words. gamma rays: ISM – ISM: supernova remnants – ISM: individual objects (SNR G78.2+2.1) – ISM: clouds – ISM: cosmic rays

1. Introduction

The supernova remnant (SNR) γ -Cygni (G78.2+2.1) is known as a puzzling γ -ray source located in the complex Cygnus region. The multi-wavelength analysis towards it from radio to γ -ray have never ceased, while the origins of its γ -ray emission has remained unconfirmed. [Ladouceur & Pineault \(2008\)](#) revealed the radio flux spectral index α_ν varies between ~ 0.8 and $\lesssim 0.4$ across the SNR. The softest index is found in the bright south-eastern part, and the north-west part is harder (~ 0.55) ([MAGIC Collaboration et al. 2023](#)). Near the center, there is an energetic GeV-bright pulsar PSR J2021+4026, for which it has been proved that the state and pulse profile vary ([Wang et al. 2023](#); [Razzano et al. 2023](#)). Also, the unknown distances make the γ -ray emission in this region more puzzling. In the VHE energy band, VERITAS suggests a $\sim 0.23^\circ$ extended source in the northwest part ([Aliu et al. 2013](#)), which is updated by an ellipse template ($0.29^\circ \times 0.19^\circ$) with photon index of $2.79 \pm 0.39_{\text{stat}} \pm 0.20_{\text{sys}}$ ([Abeysekara et al. 2018](#)), which location is roughly consistent with part of the MAGIC source, while inconsistent with 2HWC J2020+403 measured by HAWC ([Abeysekara et al. 2017b](#)). Further-

more, [MAGIC Collaboration et al. \(2023\)](#) found that there is a bright arc-like TeV source located on the west side outside the SNR, which is dim in the GeV band, and makes the origins of the γ -ray emission in this region even more puzzling.

Pulsar halos are a new type of γ -ray sources identified in recent years. As Pulsar Wind Nebulae (PWN) age, high-energy electrons and positrons may escape from the nebula and diffuse in the surrounding interstellar medium (ISM), after $\gtrsim 100$ kyr ([Giacinti et al. 2020](#)). The electrons and positrons diffusing out of the PWN produce γ -ray emission through Inverse Compton scattering of ambient photon fields ([López-Coto et al. 2022](#)). The recent detection of extended TeV emission around Geminga and Monogem ([Abeysekara et al. 2017b,a](#)), and the slow diffusion region around them, has sparked a widespread discussion about TeV halos. [Di Mauro et al. \(2020\)](#) argue that extended GeV emission can be measured with *Fermi* satellite around, while this is not confirmed by [Xi et al. \(2019\)](#). It is also noted that pulsar halos may exhibit an asymmetric morphology when the coherence length is large enough ([López-Coto & Giacinti 2018](#)). However, limited by the resolution and systematic uncertainties, an asymmetric morphology of these pulsar halos has not been confirmed by experiments yet ([Abeysekara et al. 2017a](#); [H. E. S. S. Collaboration et al. 2023](#)).

* yuanlss17@sjtu.edu.cn

** gwenael.giacinti@sjtu.edu.cn

*** liusm@swjtu.edu.cn

In this work, we conduct a comprehensive analysis of the GeV γ -ray emission towards the γ -Cygni area, utilizing 15 years of data from the *Fermi*-LAT instrument. The photon events are selected in an energy range from 100 MeV to 1 TeV, and the results are presented in Sect. 2. In Sect. 3, we present the gas observation results of $^{12}\text{CO}(J = 1-0)$ obtained from the Milky Way Imaging Scroll Painting (MWISP). Sect. 4 is dedicated to discussing potentially origins of the γ -ray emission, comparing multi-wavelength observations with theoretical expectations. Lastly, Sect. 5 provides our conclusions.

2. *Fermi*-LAT Data Reduction

In the subsequent analysis, the most recent *Fermi*-LAT (Atwood et al. 2009) Pass 8 data are collected from August 4, 2008 (Mission Elapsed Time 239557418) to August 4, 2023 (Mission Elapsed Time 712800005) to study the GeV emission around γ -Cygni. We select the data with "Source" event class "P8R3_SOURCE" (evclass=128) and event type FRONT + BACK (evtype=3), with the standard data quality selection criteria ($\text{DATA_QUAL} > 0$) & ($\text{LAT_CONFIG} == 1$), and exclude the zenith angle over 90° to avoid the earth limb contamination. To derive a better point-spread function and reduce contamination from the pulsar, photon energies are limited to between 20 GeV and 1 TeV for further morphology analysis. Additionally, events with energies between 100 MeV and 1 TeV are selected for a more detailed spectral analysis. All photon events within a $20^\circ \times 20^\circ$ region of interest (ROI) centered at the position of γ -Cygni in the incremental version of the fourth *Fermi*-LAT source catalog (4FGL-DR4; (Abdollahi et al. 2020a; Ballet et al. 2023)) are adopted for the binned maximum likelihood analysis (Mattox et al. 1996), together with the instrument response functions (IRF) "P8R3_SOURCE_V3"¹. The Galactic/isotropic diffuse background models (IEM, `gll_iem_v07.fits`)/(iso_P8R3_SOURCE_V3_v1.txt) are adopted, all sources listed in the 4FGL-DR4 catalog are included in the background model, and all sources within 7° from the center of ROI and two diffuse backgrounds above are set free, generated by the software `make4FGLxml.py`².

2.1. Timing Analysis

We performed the timing analysis to the 0.1-1000 GeV LAT data of the PSR J2021+4026 to separate its γ -ray emission from other sources in the region. We first included the LAT photons within an aperture radius of 3° , and weighted them by their probability of originating from the pulsar (using `gtsrprob` in the *Fermi*tools). The LAT photons with low weights (< 0.001) were excluded in the analysis. We assigned pulse phases to the LAT photons using the *Fermi* plugin of TEMPO2 (Hobbs et al. 2006; Edwards et al. 2006), according to the known ephemeris given in the LAT third pulsar catalog (Smith et al. 2023). This ephemeris covers the time period of MJD 54689–58175, so we only included the LAT data during this time period. The weighted pulse profile and the two-dimensional phaseogram are plotted in

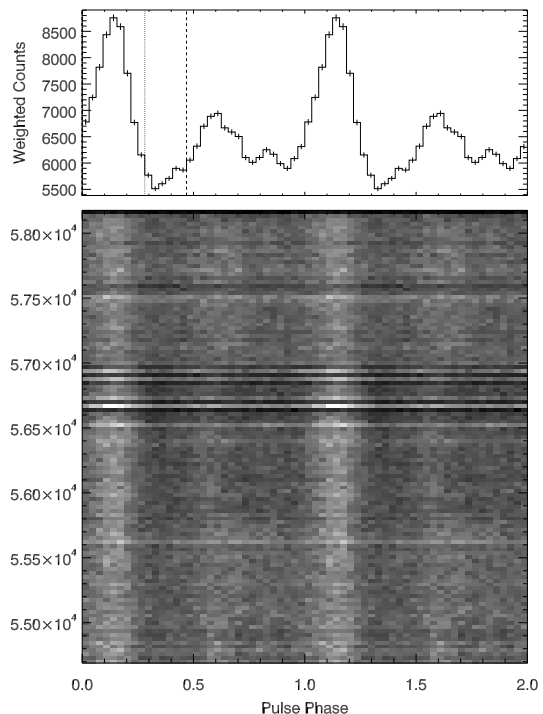


Fig. 1. Folded pulse profile and two-dimensional phaseogram in 32 phase bins derived for PSR J2021+4026. The greyscale represents the weights of photons in each bins, and the dotted and dashed lines mark the minimum and maximum phases of the off-pulse phase interval, respectively.

Figure 1. We defined the phase 0.28–0.47 as the off-pulse phase range, and the remaining phase as the on-pulse phase range.

Then we assigned pulse phases to all of the LAT events in the ROI. With LAT events during different phase ranges, we generated counts maps in different energy ranges to verify if we can avoid the contamination from PSR J2021+4026. The resulting figures are depicted as Figure 2. From the left panel of Figure 2, it can be seen that most > 10 GeV photon events (during both of the on-pulse and off-pulse phase ranges) concentrate around PSR J2021+4026. Unfortunately, significantly excess around the pulsar is still revealed when we only included events during the off-pulse phase range (the right panel of Figure 2). These results indicate that it is not enough to separate the pulsar's emission in > 10 GeV band, even though we included only the off-pulse data. Therefore, we adopted > 20 GeV data to conduct a quantitative analysis of the spatial components within the region.

2.2. Morphological analysis

In the beginning, we attempt to verify the γ -ray emission position offset with energy, and also the energy-dependent morphology. Combined with the above results, we only select photon events above 20 GeV to generate TS maps, and all TS maps are generated by only considering background fitting but not including the extended source γ -Cygni. The contribution from PSR J2021+4026 has been removed, which is described as a point-like source, whose best-fit location given by `gtfindsrc` is marked as R.A. =

¹ <http://fermi.gsfc.nasa.gov/ssc/data/access/lat/BackgroundModels.html>

² <http://fermi.gsfc.nasa.gov/ssc/data/analysis/user>

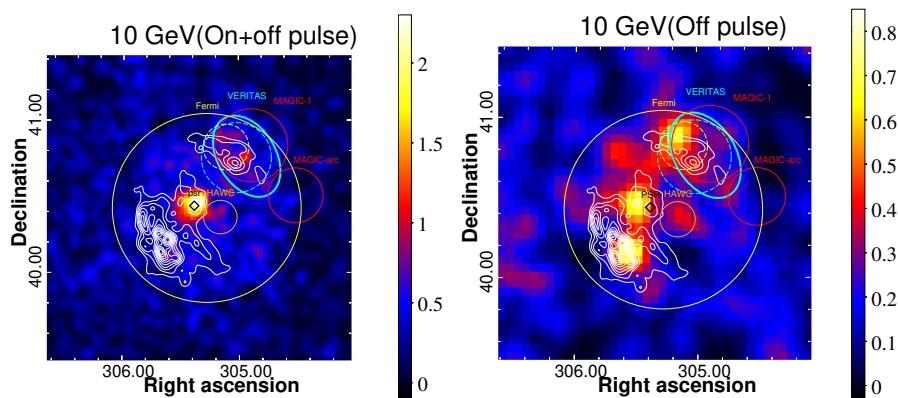


Fig. 2. Counts maps above 10 GeV extracted with the LAT data during the full (left panel) and the off-pulse (right panel) phase ranges. Labels and other details can be found in Figure 3 and Sect. 2.2.

$305.384^{\pm 0.009}^{\circ}$, Dec. = $40.441^{\pm 0.012}^{\circ}$, which is consistent with the position given by 4FGL-DR3 source list, where the extended source is described as a uniform disk with $\sigma = 0.63^{\circ}$. There are two obvious γ -ray excesses shown in the off-pulse TSmep (Figure 3 top left panel), and the potential different spectrum components inside this region (Fraija & Araya 2016), as confirmed by MAGIC Collaboration et al. (2023). Here, we then directly used two-components templates to fit the γ -ray emission in this region. First, we used a point-like source plus an extended source (Model 2 & Model 3) as our templates. Their TS values are calculated to be 839 and 846, respectively, both showing a significant improvement compared to the single disk template (Model 1). Then we further tested the two extended source scenario (Model 4), where the location of the smaller extended source is perfectly consistent with TeV observation results given by the VERITAS Collaboration (Aliu et al. 2013), and the best-fit results for the larger/smaller extended source are R.A. = 305.277° , Dec. = 40.431° , $r_{68} = 0.62^{\circ}$ and R.A. = 305.113° , Dec. = 40.832° , $r_{68} = 0.15^{\circ}$ given by Fermipy (Wood et al. 2017), and shown as yellow solid/dashed circles in Figure 3. In this scenario, the TS_{ext} for the smaller extended source is calculated to be approximately 26, rejecting the point-like source hypothesis around the 5.1σ level. The TS_{ext} is defined as $TS_{\text{ext}} = 2(\ln \mathcal{L}_{\text{ext}} - \ln \mathcal{L}_{\text{ps}})$, where \mathcal{L}_{ext} and \mathcal{L}_{ps} represent the maximum likelihood values for the extended and point-like templates, respectively. This calculation considers only one additional free parameter introduced by the extended template, and the extension significance is approximately given by $\sqrt{TS_{\text{ext}}}$ in units of σ . According to Lande et al. (2012), when $TS_{\text{ext}} > 16$, the extended source hypothesis is valid. These results suggest that the γ -ray emission in this region can be described by two extended components. To search for the correlation between GeV and TeV emission, we tested two other templates that also include two components but directly adopted the location/extension parameters from the VERITAS results. They are labeled as Model 5/Model 6, and represented by the best-fit 0.62° Gaussian template plus 0.23° circle given by Aliu et al. (2013) or $0.29^{\circ} \times 0.19^{\circ}$ ellipse given by Abeysekara et al. (2018), respectively, and they are shown as a cyan dashed circle and a solid ellipse in Figure 3. Then we also tested the 0.62° Gaussian template plus two extended components presented by MAGIC (MAGIC Collaboration et al. 2023), labeled as Model 7, and shown as red circles in Figure 3. Lastly, it is necessary to test if there

are still other spectral components that are missed. Thus we added an additional extended source into Model 4 to fit three Gaussian components simultaneously, also using Fermipy package to derive its best-fit extension and location, but its TS value did not increase (Model 8). The results are summarized in Table 1. In that table, the AIC value is defined as $AIC = 2k - 2 \ln \mathcal{L}$ and described in Akaike (1974), where k is the number of degrees of freedom of the model and \mathcal{L} is the likelihood value. The model with the minimum AIC value is preferred, thus we adopted Model 4 for the following spectral analysis.

2.3. Energy Spectrum

In Section 2.2, Model 4 has the best performance and it is adopted here for further spectral analyses. Hereafter, the 0.62° Gaussian source, spatially corresponding to the whole SNR region, is named as Src_{Fermi} . The 0.15° Gaussian source is spatially corresponding to the VERITAS region, and is named as Src_{VERITAS} . After using events from 100 MeV to 1 TeV, we obtained different spectral types like simple power-law (PL; $dN/dE \propto E^{-\alpha}$) and broken power-law (BPL³), and the results are then summarized in Table 2. For the Src_{Fermi} , the BPL model does not provide a notable improvement of the fitting quality compared with a PL assumption. This could be quantified as TS_{curve} , defined as $TS_{\text{curve}} = 2(\ln \mathcal{L}_{\text{BPL}} - \ln \mathcal{L}_{\text{PL}})$ (Abdollahi et al. 2020b), and the derived value of 4.1 corresponds to a significance level of $\sim 2.0 \sigma$. Thus we suggest that there is no energy break in the Src_{Fermi} spectrum. For the Src_{VERITAS} , its $TS_{\text{curve}} = 3.6$ is even lower than 2σ and its calculated TS value shows barely any difference between a PL and a BPL assumption. Thus we suggest that its spectrum can also be described by a single PL. Then we obtained their spectral energy distributions (SEDs) by separating the events in the 100 MeV - 1 TeV energy range into twelve logarithmically equal intervals and repeated the likelihood evaluation analysis for each interval. In this part, the normalization values of all sources are left free, and others parameters are fixed. For bins having TS values lower than 5.0, we calculated the upper limits using a Bayesian method (Helene 1983) at a 95% confidence level.

$${}^3 dN/dE \propto \begin{cases} \left(\frac{E}{E_b}\right)^{-\Gamma_1}, & E < E_b \\ \left(\frac{E}{E_b}\right)^{-\Gamma_2}, & E > E_b \end{cases}$$

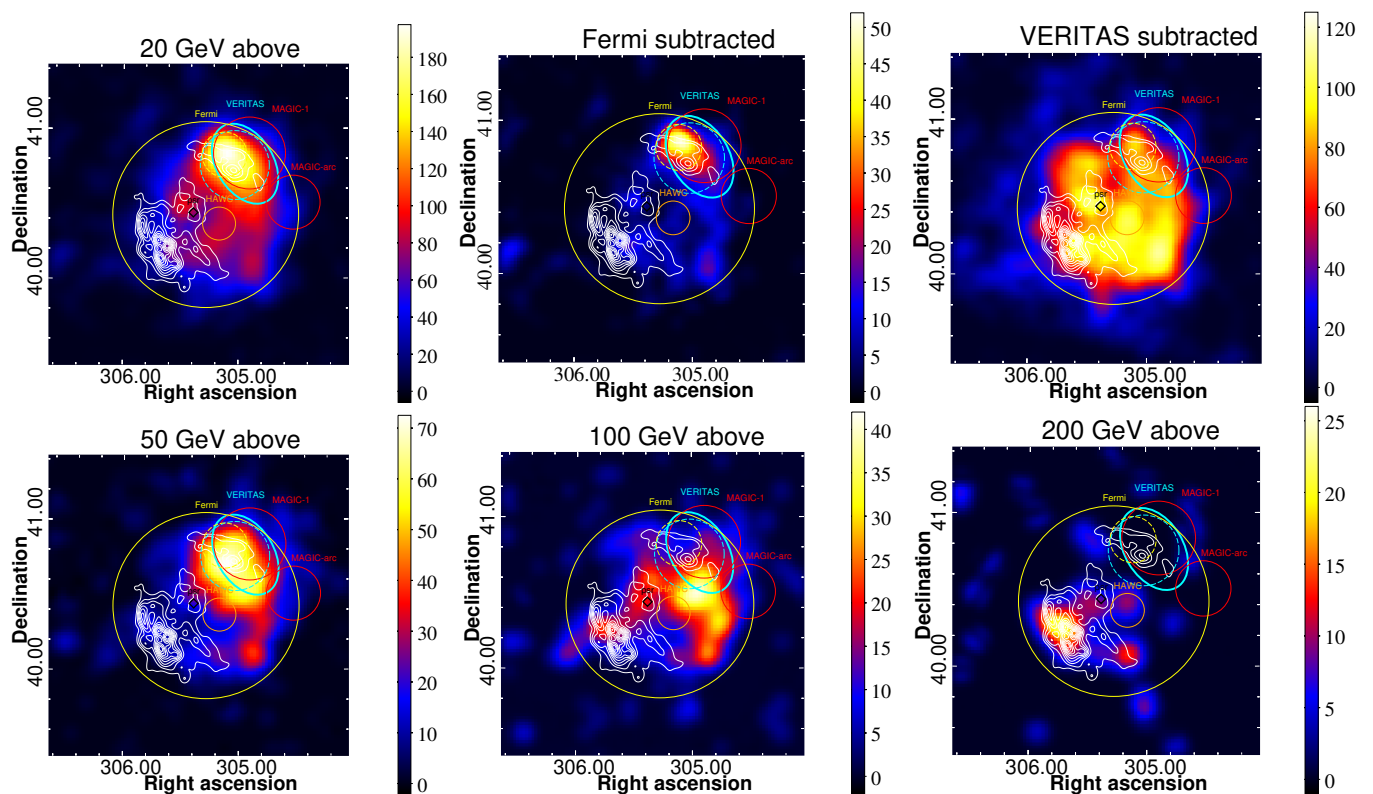


Fig. 3. TS maps in the vicinity of γ -Cygni observed with the *Fermi*-LAT. The energy range for each sub-figure is shown above them. The yellow solid/dashed circle shows the best-fit extension with r_{68} of two Gaussian template in this work given by *Fermi*-LAT. The red circles show the two extended emission measured by MAGIC (MAGIC Collaboration et al. 2023), and part of the smaller circle spatially corresponds to the MAGIC-arc region. The cyan circle/ellipse shows the 2013/2018 VERITAS results (Aliu et al. 2013; Abeysekara et al. 2018), respectively. The orange circle shows the center of HAWC source with 1σ error radius (Abeysekara et al. 2017b). The black diamond shows the position of gamma-ray pulsar PSR J2021+4026. The white contours come from the CGPS 1420 MHz radio intensity (Ladouceur & Pineault 2008), and represent the two brightest regions in the SNR shell.

Table 1. Spatial models tested for the GeV γ -ray emission above 20 GeV

Morphology(>20GeV)	TS	Best-fit Extension(R_{68})	σ	Ndf ^a	ΔAIC ^b
Model 1 (4FGL-DR3)	770	0.517°	0.63°	5	0
Model 2 (Point + Disk)	839	0.47°	0.57°	9	-61
Model 3 (Point + Gaussian)	846	0.58°	0.38°	9	-68
Model 4 (Two Gaussians)	872	$0.62^\circ(0.15^\circ)$	$0.41^\circ(0.10^\circ)$	10	-92
Model 5 (Fermi + VERITAS circle fixed)	859	$0.62^\circ(0.23^\circ)$	$0.41^\circ(0.15^\circ)$	4	-91
Model 6 (Fermi + VERITAS ellipse fixed)	857	$0.62^\circ(0.29^\circ \times 0.19^\circ)$	$0.41^\circ(-)$	4	-89
Model 7 (Fermi + MAGIC fixed)	847	$0.62^\circ(0.24^\circ, 0.18^\circ)$	$0.41^\circ(0.16^\circ, 0.12^\circ)$	4	-79
Model 8 (Three Gaussians)	869	$0.63^\circ(0.17^\circ, 0.21^\circ)$	$0.42^\circ(0.11^\circ, 0.14^\circ)$	15	-79

Notes. ^(a) Degrees of freedom. ^(b) Calculated with respect to Model 1.

Table 2. Spectral fit parameters in 100 MeV - 1 TeV

Sources	Spectral type	Γ_1	Γ_2	$E_b(\text{GeV})$	Photon flux(photon $\text{cm}^{-2} \text{s}^{-1}$)	TS
Src _{Fermi}	PL	2.149 ± 0.005	—	—	$(3.31 \pm 0.08) \times 10^{-7}$	8670
Src _{Fermi}	BPL	1.683 ± 0.008	2.171 ± 0.006	1.6 ± 0.7	$(3.22 \pm 0.07) \times 10^{-7}$	8674
Src _{VERITAS}	PL	2.01 ± 0.06	—	—	$(2.34 \pm 0.42) \times 10^{-8}$	223
Src _{VERITAS}	BPL	1.94 ± 0.11	2.02 ± 0.08	3.4 ± 2.9	$(2.41 \pm 0.65) \times 10^{-8}$	226

3. CO observations

We make use of the data from the Milky Way Imaging Scroll Painting (MWISP⁴) project with high resolution CO survey along the Northern Galactic plane with the Purple

⁴ <http://english.dlh.pmo.cas.cn/ic/>

Mountain Observatory (PMO) 13.7 m telescope (Su et al. 2019). In this part, given that the HI emission at velocities between $[-19.0, -11.0] \text{ km s}^{-1}$ measured by CGPS (Ladouceur & Pineault 2008) is likely associated with remnants, and the average HI spectrum shows that the cloud might be disturbed by the shock front in the velocity range

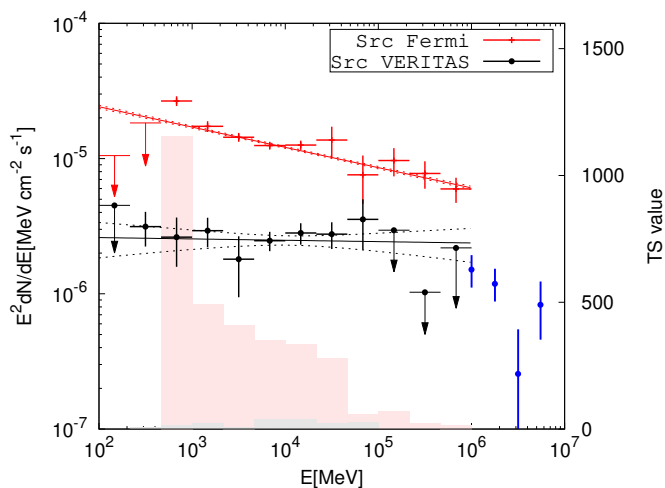


Fig. 4. γ -ray SED obtained from the events in 0.1-1000 GeV. The red/black solid line shows the best-fit PL spectral for each component. The dotted lines show the 68% confidence bands. The blue data points are the VERITAS results (Abeysekara et al. 2018). The histogram denotes the TS value for each bin.

$[-16.0, +16.0]$ km s^{-1} (see also Figure 37, 38 and 39 in Ladouceur & Pineault (2008)), we integrated the radial velocity range $[-16.0, -11.0]$ km s^{-1} and $[+9.0, +12.0]$ km s^{-1} to calculate the molecular hydrogen column mass, respectively. Here we assume the association between molecular cloud and γ -Cygni, then adopted the distance $d = 1.5$ kpc into further calculations (which are derived from the assumption that γ -Cygni is associated with the nearby star-forming region, while in the Cygnus region direction, we cannot simply obtain the actual distance through velocity). Under the assumption of $\theta = 0.62^\circ$, the obtained physical radius is ~ 16.2 pc. To determine the column density of H_2 in this region, we employ a conversion factor $X_{\text{CO}} = 2 \times 10^{20} \text{ cm}^{-2} \text{ K}^{-1} \text{ km}^{-1} \text{ s}$ (Bolatto et al. 2013; Dame et al. 2001). Using this factor, the column density N_{H_2} is calculated as $N_{\text{H}_2} = X_{\text{CO}} \times W_{\text{CO}}$. Consequently, the mass of the molecular complex can be derived from the W_{CO} :

$$M = \mu m_{\text{H}} D^2 \Delta \Omega_{\text{px}} X_{\text{CO}} \sum_{\text{px}} W_{\text{CO}} \propto N_{\text{H}_2}, \quad (1)$$

In this formula, μ is set to 2.8, reflecting a relative helium abundance of 25%. The mass of a hydrogen nucleon is denoted as m_{H} . The total column density of hydrogen atoms in each pixel is represented by $N_{\text{H}} = 2N_{\text{H}_2}$. The solid angle subtended by each pixel is given by $\Delta \Omega_{\text{px}}$. The term $\sum_{\text{px}} W_{\text{CO}}$ accounts for the velocity binning of the data cube. It is calculated by summing the map content for the pixels within the target sky region and the specified velocity range, and then scaling by the velocity bin size.

As shown in the left panel of Figure 5, in the velocity range $[+9.0, +12.0]$ km s^{-1} , only the VERITAS source region exhibits a spatial correspondence between the gas distribution and the location of the γ -ray emission. The cyan circle indicates the radius of $\text{Src}_{\text{VERITAS}}$. Since part of the molecular cloud (MC) is located outside the projection radius of $\text{Src}_{\text{VERITAS}}$, the magenta circle is used to calculate the total MC mass in this velocity range, which includes the MC mass potentially interacting with the escaped CRs.

In the right panel of Figure 5, within the velocity range of $[-16.0, -11.0]$ km s^{-1} , the brightest part of the SNR shell in the southeast shows good spatial coincidence with the gas distribution. The red circle denotes the total MC mass in this velocity range, and the orange circle indicates the radius of the HAWC source measurement. Details about their correlation can be found in Sect. 4. Combined with the HI spectrum, which also supports the association between the SNR and the gas in this velocity range (MAGIC Collaboration et al. 2023; Ladouceur & Pineault 2008), we calculate the density and mass of each cloud to derive a more precise normalization factor for the subsequent hadronic model.

Hereafter, the cyan, orange, magenta and red spherical regions are named as Cloud i ($i = \text{veritas, hawc, shockV, shockH}$), respectively. Notably, within the HAWC source region, only weak γ -ray excess is detected above 100 GeV. By using the estimation made for N_{H_2} , the mass of the molecular cloud within 0.15° of $\text{Clump}_{\text{veritas}}$ is calculated to be about $M_{\text{veritas}} = 102 d_{1.5}^2 M_{\odot}$. Assuming a spherical geometry of the gas distribution, we estimate the volume to be $V_{\text{veritas}} = \frac{4\pi}{3} R^3$, where $R = d \times \theta$, and the average H_2 cubic density in this region is about $n_{\text{veritas}} = 16 d_{1.5}^{-1} \text{ cm}^{-3}$. Correspondingly, the gas mass within each other spherical regions can be calculated as $M_{\text{hawc}} = 63 d_{1.5}^2 M_{\odot}$, $M_{\text{shockV}} = 171 d_{1.5}^2 M_{\odot}$, $M_{\text{shockH}} = 542 d_{1.5}^2 M_{\odot}$. Therefore, we can subtract the two to obtain the remaining gas mass in each velocity range, denoted as $M_{\text{escapeH}} = M_{\text{shockH}} - M_{\text{hawc}} = 479 d_{1.5}^2 M_{\odot}$ and $M_{\text{escapeV}} = M_{\text{shockV}} - M_{\text{veritas}} = 69 d_{1.5}^2 M_{\odot}$. Considering the radius of each spherical region, their densities are calculated to be around several tens of cm^{-3} . To be more precise, they fluctuate between approximately $4 d_{1.5}^{-1} \text{ cm}^{-3}$ and $29 d_{1.5}^{-1} \text{ cm}^{-3}$.

4. Discussion of the possible origins of the γ -ray emission

4.1. SNR-MC Interaction

The MC have a good spatial correspondence with the brightest GeV excess location and part of the SNR shell around the VERITAS source region. Another clump spatially coincides with the brightest SNR shell structure and the γ -ray emission above 200 GeV. Considering their spectrum measured by *Fermi*-LAT, we suggest that both the north-west and south-east shock fronts interacted with nearby dense gas, like RX J1713.7-3946 (Sano et al. 2013; Tanaka et al. 2020), and the SNR-MC interaction occurring in the lower density environment results in a harder spectral index (Yuan et al. 2012). This scenario corresponds to part of an SNR shell interacting with molecular clouds of varying densities, leading to inhomogeneous γ -ray emission. In this scenario, the soft component in the lower GeV energy band can be interpreted as escaped CRs illuminating nearby MCs, even if their projected positions are located within the SNR shell (Li et al. 2023). The flat component, on the other hand, can be attributed to trapped ions originating from shocks interacting with the gas complex. Furthermore, the different mass ratios of MCs inside the trapped zone compared to the escaped emission zone would result in varying γ -ray flux amplitudes across different interaction regions.

Here, we consider a scenario where protons are injected instantaneously into a uniformly emitting region called

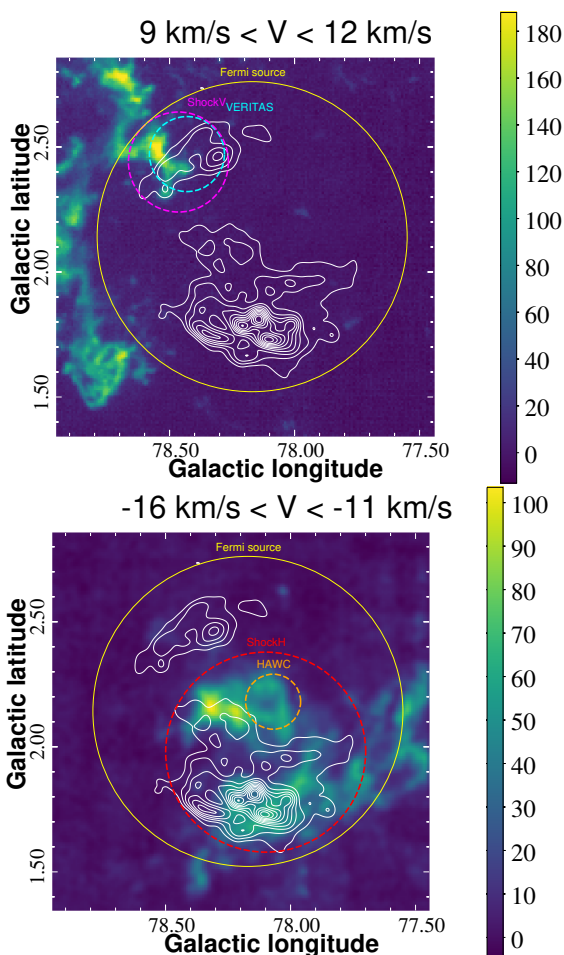


Fig. 5. Integrated ^{12}CO ($J = 1-0$) emission intensity (K km s^{-1}) toward γ -Cygni region in the velocity ranges $[+9.0, +12.0]$ km s^{-1} (left panel) and $[-16.0, -11.0]$ km s^{-1} (right panel) using MWISP data. The labels are the same as in Figure 3. Cyan, magenta, red and orange circles correspond to different cloud spherical regions, respectively.

Zone S (corresponding to $\text{Clump}_{\text{shockV}}$ and $\text{Clump}_{\text{shockH}}$), approximately 7000 years ago and the spectrum of the injected protons can be characterized as a broken power-law spectrum:

$$Q(E) = Q_0 \frac{(E/E_{p,\text{break}})^{-\gamma_1}}{1 + (E/E_{p,\text{break}})^{\gamma_2 - \gamma_1}} \quad (2)$$

$E_{p,\text{break}}$ represents the break energy, γ_1 and γ_2 being the spectral indices below and above the energy break, respectively. Because of the flat γ -ray spectrum ~ 2.0 in the GeV energy band for the VERITAS region, we set $\gamma_1 = 2.0$ for simplicity and $\gamma_2 = \gamma_1 + 1.0$ (Zeng et al. 2019). $E_{p,\text{break}}$ is fixed to 5 TeV, and then the distribution of the escaped protons in the emission region can be calculated following the method outlined by Liu et al. (2020):

$$N_p(E, r_s, T) = \frac{Q(E)}{[4\pi D(E)T]^{\frac{3}{2}}} \int_0^R 4\pi r^2 dr \exp\left[\frac{-r_s^2}{4D(E)T}\right] \quad (3)$$

The diffusion coefficient is assumed to be uniform, following the form $D(E) = \chi D_0 (E/E_0)^\delta$ for $E > E_0$, where $D_0 =$

$1 \times 10^{28} \text{ cm}^2 \text{ s}^{-1}$ at $E_0 = 10 \text{ GeV}$ and $\delta = 1/2$, consistent with Kraichnan turbulence (Kraichnan 1965; Blasi 2013). Due to projection effects, the actual distance between the gas complex and the supernova remnant (SNR) remains uncertain. Furthermore, in the Cygnus region direction, the relationship between kinematic distance and gas velocity can no longer be derived by the method described in Reid et al. (2009, 2014), thus we adopted r_s as a free parameter representing the distance between the injection site and the illuminated molecular clouds. With the injected source spectrum defined by $Q(E) \propto E^{-\Gamma}$ and $D(E) \propto E^\delta$, equation 3 reveals that $N_p(E)$ will show a lower energy spectral cutoff at $E_{p,\text{break}}$ when $\sqrt{4D(E_b)T} \simeq r_s$. Correspondingly, $N_p(E)$ will follow $N_p(E) \propto E^{-(\Gamma + \frac{3}{2}\delta)}$. The total energy of injected protons is denoted as $W_{\text{inj}} = \eta E_{\text{SN}}$, where η is the efficiency of converting kinetic energy into accelerated protons, typically valued at 0.1. The kinetic energy of the SNR, E_{SN} is generally taken to be 10^{51} erg (Blasi 2013). Additionally, the correction factor χ for the diffusion coefficient is set to 1.0 corresponding to the standard value of the Galactic diffusion coefficient (Blasi 2013). The corresponding γ -ray fluxes produced in the emission zone are then calculated with the *naima* package (Zabalza 2015).

For the total γ -Cygni region, the resulting γ -ray flux can be well described by adding the escaped ions together with the trapped ions contribution, shown as red and orange dashed lines in the left panel of Figure 6. The total energy of escaped and trapped protons above 1 GeV are calculated to be $W_{\text{escapedH}} = 6.32 \times 10^{48} (M_{\text{escapeH}}/479M_\odot)^{-1} \text{ erg}$ and $W_{\text{trappedH}} = 8.98 \times 10^{49} (M_{\text{hawc}}/63M_\odot)^{-1} \text{ erg}$, respectively. As mentioned above, assuming a distance of 1.5 kpc, the source radius is calculated to be $r_s = 16.2 \text{ pc}$. However, the precise value for r_s cannot be constrained due to the projection effect, thus we add four scenarios where $r_s = 10/20/30/40 \text{ pc}$ to show the dependence between r_s and the γ -ray flux, and plot the results in the middle panel in Figure 6. For the VERITAS region, we suggest that its GeV emission with a flat spectrum is mainly dominated by the happening shock-cloud interactions (Liu et al. 2022), shown as a cyan dashed line, while the escaped component also has a contribution. However, due to the low ratio value of the gas densities between the escaped emission zone and the trapped zone, the escaped component can only have a low contribution, see the magenta dashed line. Correspondingly, the high ratio value of gas densities between escaped zone and trapped zone would lead to a higher escaped γ -ray flux component in the lower energy band, similar to the left panel in Figure 6. The total energy of each part can be calculated as $W_{\text{escapedV}} = 4.77 \times 10^{48} (M_{\text{escapeV}}/69M_\odot)^{-1} \text{ erg}$ and $W_{\text{trappedV}} = 4.31 \times 10^{49} (M_{\text{veritas}}/102M_\odot)^{-1} \text{ erg}$.

4.2. Pulsar Wind Nebula and Pulsar halo

Considering the presence of the detected GeV-bright pulsar, the γ -ray emission in this region might be powered by high-energy electrons and positrons generated by a pulsar wind nebula (PWN). Like, e.g., MSH 15 - 52 (H. E. S. S. Collaboration et al. 2018) and HESS J1825 - 137 (Principe et al. 2020), typical γ -ray PWNe detected by *Fermi*-LAT are always driven by energetic pulsars with higher \dot{E} between $10^{36} \sim 10^{39} \text{ erg s}^{-1}$ (Acero et al. 2013). The value of $10^{35} \text{ erg s}^{-1}$ is at least one order of magnitude lower, and

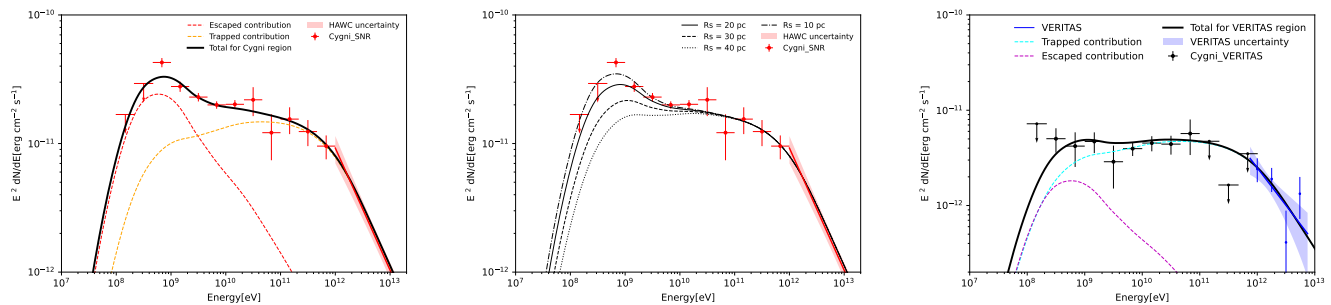


Fig. 6. Modeling of the γ -ray spectrum in the hadronic scenario. Left panel: The black solid line shows the total contribution from the sum of the red and orange dashed lines, corresponding to the escaped and trapped ions, respectively. The red butterfly is extracted from Abeysekara et al. (2017b). Middle panel: Total γ -ray contribution calculated with different r_s . Right panel: Predicted γ -ray flux in the VERITAS region, by adding the escaped and trapped components. Blue data points and butterfly come from Abeysekara et al. (2018).

thus the scenario of it being the origin of the γ -ray emission in the γ -Cygni region is disfavored.

We now determine if the TeV emission can be interpreted as Inverse Compton scattering of ambient photon fields by relativistic electrons and positrons that have escaped from a potential PWN and diffuse into the ISM (López-Coto et al. 2022), leading to a pulsar halo around the pulsar. To do so, we adopt here the two different approaches depicted in Giacinti et al. (2020) to estimate the energy density ε_e from the pulsar properties and the γ -ray luminosity. The region $\varepsilon_e \ll \varepsilon_{\text{ISM}}$ (area shaded in gray in Figure 7) corresponds to when the energy density in the relativistic electrons and positrons is negligible compared with that of the ISM. This corresponds to the region where pulsar halos may form. In contrast, $\varepsilon_e \gtrsim \varepsilon_{\text{ISM}}$ corresponds to the case when the emitting electrons would be contained in the region that is dynamically dominated by the pulsar (Giacinti et al. 2020).

To present a more intuitive comparison, we also included the identified pulsar halo LHAASO J0622+3749 (Aharonian et al. 2021) in our figure, represented by a star symbol, located near Geminga and PSR B0656+14 (Abeysekara et al. 2017a). Its parameters are summarized in Table 3. For the γ -Cygni region, we adopted the TeV extension size of $\theta = 0.23^\circ$ in our calculations. Since the distance to the pulsar is unknown, we considered 1.0 kpc and 2.0 kpc as the minimum and maximum distances, assuming PSR J2021+4026 is associated with the SNR. The corresponding radii for each scenario are 4.014 pc and 8.028 pc, respectively, and they are shown with different squares in the Figure 7. From the lower panel of Figure 7, it is hard to definitively attribute the TeV emission to a potential pulsar halo. However, we note that the green square, representing the larger distance (2.0 kpc), is situated near the boundary of shadow region, but not within it. Considering that the pulsar’s age is only 77 kyr, we suggest that this source might be in an intermediate stage of transitioning from a PWN to a pulsar halo. This implies that the halo has not yet fully formed, causing its \dot{E} and ε_e to fall between those of a typical PWN and a mature pulsar halo. Additionally, we observe that the calculated $\varepsilon_e(L_\gamma)$ is approximately 0.17 eV/cm^3 under the 2.0 kpc assumption. This suggests that even if the actual distance is much greater (e.g., 4.0 kpc), the energy density would not decrease sufficiently to fall entirely within the shaded area. These results contrast sharply

with those for the three identified pulsar halos shown with stars in Figure 7, which are all located in the shaded areas in the bottom panels. In the meantime, numerical simulations suggest that the morphology of a pulsar halo can exhibit highly asymmetric and distorted shapes, especially when the coherence length of the interstellar turbulence exceeds 10 pc (López-Coto & Giacinti 2018). Furthermore, Bao et al. (2024) shows an offset between the brightest TeV excess and pulsar position. This implies that, in extreme cases, the actual extent of the halo may be difficult to measure due to the filamentary structure caused by asymmetric diffusion of cosmic rays (Giacinti et al. 2012, 2013). Therefore, further investigations of this region using high-resolution detectors across other wavelengths are essential to better constrain the parameter space, such as e.g. the magnetic field strength and its direction.

5. Conclusions

We analyzed the γ -ray emission in the vicinity of γ -Cygni using 15 years of *Fermi*-LAT data, and confirmed that the GeV counterpart of the VERITAS source is quite different from other parts inside the SNR. Given that the molecular cloud clump in this region spatially coincides with part of the GeV emission and the radio shell, we suggest that the flatter component could be attributed to trapped ions, while the low-energy soft component may be due to escaped cosmic rays interacting with nearby molecular clouds. The GeV spectrum of γ -Cygni, therefore, consists of a mixture of these two components. The varying gas density ratios between the escaped emission zone and the trapped zone result in different γ -ray flux amplitudes across different regions. On the other hand, considering the high spin-down luminosity of the central γ -ray pulsar PSR J2021+4026, we estimated its energy density ε_e using two approaches as shown in Giacinti et al. (2020). The calculated results support the SNR scenario and rule out the pulsar halo hypothesis. However, in combination with recent numerical simulation work (López-Coto & Giacinti 2018; Bao et al. 2024), we suggest that the possibility of the SNR overlapping with a twisted-morphology pulsar halo scenario cannot be entirely ruled out.

Acknowledgements. This research made use of the data from the Milky Way Imaging Scroll Painting (MWISP) project, which is a multi-line survey in 12CO/13CO/C18O along the northern galactic

Table 3. Comparison of the properties of pulsar halo J0622+3749 and γ -Cygni with different distance assumptions

Name	P (s)	\dot{P} (10^{-14} s s $^{-1}$)	L_{sd} (10^{34} erg s $^{-1}$)	τ (kyr)	d (kpc)	R^a (pc)	B^b (10^{12} G)	$\varepsilon_e(\dot{E})$ (eV/cm 3)	$\varepsilon_e(L_\gamma)$ (eV/cm 3)
J0622+3749	0.333	2.542	2.7	207.8	1.60	11.17	3.0	0.644	0.008
Cygni near/far	0.265	0.348	10.0	77.0	1.0/2.0	4.01/8.02	4.0	19.05/2.38	0.34/0.17

Notes. (a) Radius. (b) Magnetic field.

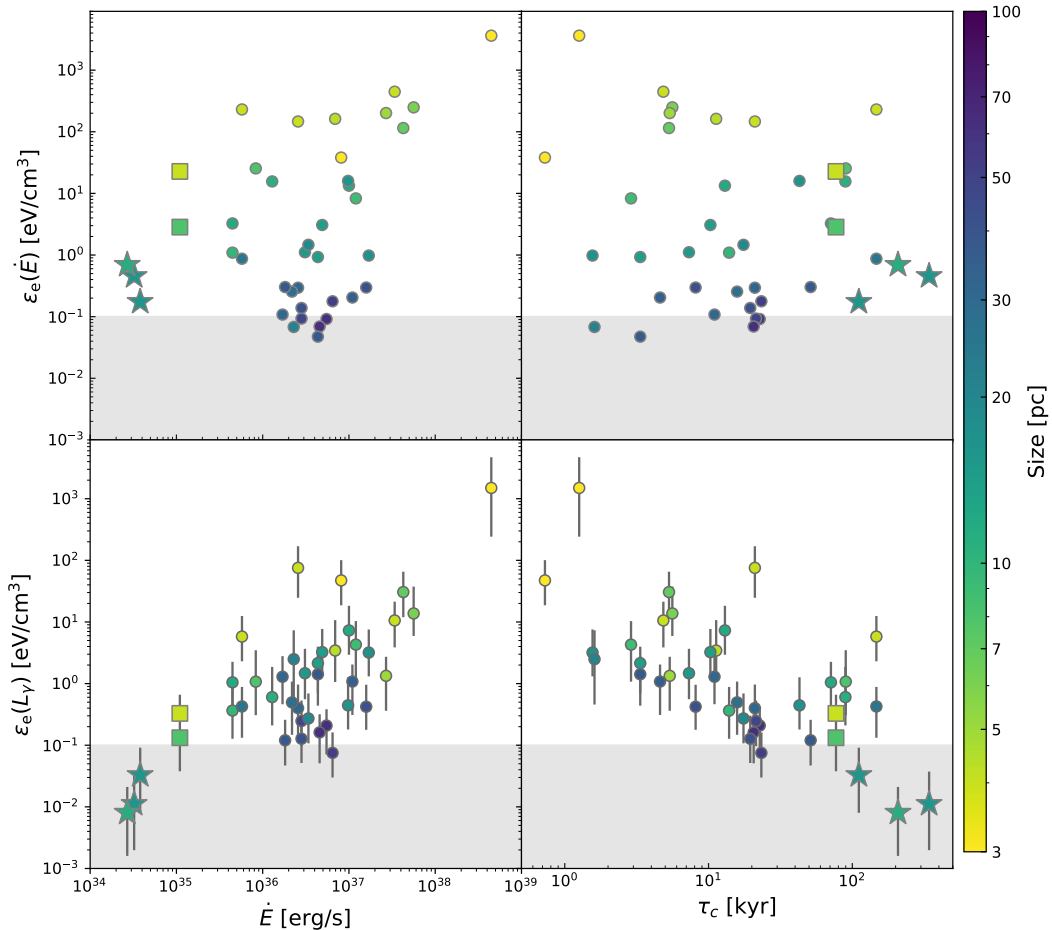


Fig. 7. Energy density of TeV sources calculated using two different approaches. The top panels are calculated as $\varepsilon_e = \dot{E}\tau_c/V$, and the bottom panels are calculated following the approach in Section 3.2 of Giacinti et al. (2020). The newly identified pulsar halo associated with PSR J0622+3749 (Aharonian et al. 2021), indicated by a star, is shown along with the halos of Geminga and Monogem (shown as stars, too). γ -Cygni under different distance assumptions is shown as squares.

plane with PMO-13.7m telescope. We are grateful to all the members of the MWISP working group, particularly the staff members at PMO-13.7m telescope, for their long-term support. MWISP was sponsored by National Key R&D Program of China with grants 2023YFA1608000 & 2017YFA0402701 and by CAS Key Research Program of Frontier Sciences with grant QYZDJ-SSW-SLH047. We also would like to thank P.P.Delia, Yang Su for invaluable discussions. This work is supported by the National Natural Science Foundation of China under the grants No. 12393853, U1931204, 12103040, 12147208, and 12350610239, the Natural Science Foundation for Young Scholars of Sichuan Province, China (No. 2022NSFSC1808), and the Fundamental Research Funds for the Central Universities (No. 2682022ZTPY013).

References

- Abdollahi, S., Acero, F., Ackermann, M., et al. 2020a, ApJS, 247, 33
Abdollahi, S., Acero, F., Ackermann, M., et al. 2020b, ApJS, 247, 33
Abeyssekara, A. U., Albert, A., Alfaro, R., et al. 2017a, Science, 358, 911
Abeyssekara, A. U., Albert, A., Alfaro, R., et al. 2017b, ApJ, 843, 40
Abeyssekara, A. U., Archer, A., Aune, T., et al. 2018, ApJ, 861, 134
Acero, F., Ackermann, M., Ajello, M., et al. 2013, ApJ, 773, 77
Aharonian, F., An, Q., Axikegu, Bai, L. X., et al. 2021, Phys. Rev. Lett., 126, 241103
Akaike, H. 1974, IEEE Transactions on Automatic Control, 19, 716
Aliu, E., Archambault, S., Arlen, T., et al. 2013, ApJ, 770, 93
Atwood, W. B., Abdo, A. A., Ackermann, M., et al. 2009, ApJ, 697, 1071

- Ballet, J., Bruel, P., Burnett, T. H., Lott, B., & The Fermi-LAT collaboration. 2023, arXiv e-prints, arXiv:2307.12546
- Bao, Y., Giacinti, G., Liu, R.-Y., Zhang, H.-M., & Chen, Y. 2024, arXiv e-prints, arXiv:2407.02478
- Blasi, P. 2013, *A&A Rev.*, 21, 70
- Bolatto, A. D., Wolfire, M., & Leroy, A. K. 2013, *ARA&A*, 51, 207
- Dame, T. M., Hartmann, D., & Thaddeus, P. 2001, *ApJ*, 547, 792
- Di Mauro, M., Manconi, S., & Donato, F. 2020, *Phys. Rev. D*, 101, 103035
- Edwards, R. T., Hobbs, G. B., & Manchester, R. N. 2006, *MNRAS*, 372, 1549
- Fraija, N. & Araya, M. 2016, *ApJ*, 826, 31
- Giacinti, G., Kachelrieß, M., & Semikoz, D. V. 2012, *Phys. Rev. Lett.*, 108, 261101
- Giacinti, G., Kachelrieß, M., & Semikoz, D. V. 2013, *Phys. Rev. D*, 88, 023010
- Giacinti, G., Mitchell, A. M. W., López-Coto, R., et al. 2020, *A&A*, 636, A113
- H. E. S. S. Collaboration, Abdalla, H., Abramowski, A., et al. 2018, *A&A*, 612, A2
- H. E. S. S. Collaboration, Aharonian, F., Ait Benkhali, F., et al. 2023, *A&A*, 673, A148
- Helene, O. 1983, *Nuclear Instruments and Methods in Physics Research*, 212, 319
- Hobbs, G. B., Edwards, R. T., & Manchester, R. N. 2006, *MNRAS*, 369, 655
- Kraichnan, R. H. 1965, *Physics of Fluids*, 8, 1385
- Ladouceur, Y. & Pineault, S. 2008, *A&A*, 490, 197
- Lande, J., Ackermann, M., Allafort, A., et al. 2012, *ApJ*, 756, 5
- Li, Y., Liu, S., & He, Y. 2023, *ApJ*, 953, 100
- Liu, S., Zeng, H., Xin, Y., & Zhang, Y. 2022, *Reviews of Modern Plasma Physics*, 6, 19
- Liu, S., Zeng, H., Xin, Y., & Zhu, H. 2020, *ApJ*, 897, L34
- López-Coto, R., de Oña Wilhelmi, E., Aharonian, F., Amato, E., & Hinton, J. 2022, *Nature Astronomy*, 6, 199
- López-Coto, R. & Giacinti, G. 2018, *MNRAS*, 479, 4526
- MAGIC Collaboration, Acciari, V. A., Ansoldi, S., et al. 2023, *A&A*, 670, A8
- Mattox, J. R., Bertsch, D. L., Chiang, J., et al. 1996, *ApJ*, 461, 396
- Principe, G., Mitchell, A. M. W., Caroff, S., et al. 2020, *A&A*, 640, A76
- Razzano, M., Fiori, A., Saz Parkinson, P. M., et al. 2023, *A&A*, 676, A91
- Reid, M. J., Menten, K. M., Brunthaler, A., et al. 2014, *ApJ*, 783, 130
- Reid, M. J., Menten, K. M., Zheng, X. W., et al. 2009, *ApJ*, 700, 137
- Sano, H., Tanaka, T., Torii, K., et al. 2013, *ApJ*, 778, 59
- Smith, D. A., Abdollahi, S., Ajello, M., et al. 2023, *ApJ*, 958, 191
- Su, Y., Yang, J., Zhang, S., et al. 2019, *ApJS*, 240, 9
- Tanaka, T., Uchida, H., Sano, H., & Tsuru, T. G. 2020, *ApJ*, 900, L5
- Wang, H. H., Takata, J., Lin, L. C. C., & Tam, P. H. T. 2023, arXiv e-prints, arXiv:2307.03661
- Wood, M., Caputo, R., Charles, E., et al. 2017, in *International Cosmic Ray Conference*, Vol. 301, 35th International Cosmic Ray Conference (ICRC2017), 824
- Xi, S.-Q., Liu, R.-Y., Huang, Z.-Q., Fang, K., & Wang, X.-Y. 2019, *ApJ*, 878, 104
- Yuan, Q., Liu, S., & Bi, X. 2012, *ApJ*, 761, 133
- Zabalza, V. 2015, in *International Cosmic Ray Conference*, Vol. 34, 34th International Cosmic Ray Conference (ICRC2015), 922
- Zeng, H., Xin, Y., & Liu, S. 2019, *ApJ*, 874, 50